Converged *GW* quasiparticle energies for transition metal oxide perovskites

Zeynep Ergönenc, Bongjae Kim, Peitao Liu, Georg Kresse, and Cesare Franchini*
Faculty of Physics, Computational Materials Physics, University of Vienna, Vienna A-1090, Austria

(Received 6 December 2017; published 5 February 2018)

The *ab initio* calculation of quasiparticle (QP) energies is a technically and computationally challenging problem. In condensed matter physics, the most widely used approach to determine QP energies is the *GW* approximation. Although the *GW* method has been widely applied to many typical semiconductors and insulators, its application to more complex compounds such as transition metal oxide perovskites has been comparatively rare, and its proper use is not well established from a technical point of view. In this work, we have applied the single-shot G_0W_0 method to a representative set of transition metal oxide perovskites including 3*d* ($SrTiO_3$, $LaScO_3$, $SrMnO_3$, $LaTiO_3$, $LaVO_3$, $LaCrO_3$, $LaMnO_3$, and $LaFeO_3$), 4*d* ($SrZrO_3$, $SrTcO_3$, and Ca_2RuO_4), and 5*d* ($SrHfO_3$, $KTaO_3$, and $NaOsO_3$) compounds with different electronic configurations, magnetic orderings, structural characteristics, and band gaps ranging from 0.1 to 6.1 eV. We discuss the proper procedure to obtain well-converged QP energies and accurate band gaps within single-shot G_0W_0 by comparing the conventional approach based on an incremental variation of a specific set of parameters (number of bands, energy cutoff for the plane-wave expansion and number of **k** points) and the basis-set extrapolation scheme [J. Klimeš *et al.*, Phys. Rev. B **90**, 075125 (2014)]. Although the conventional scheme is not supported by a formal proof of convergence, for most cases it delivers QP energies in reasonably good agreement with those obtained by the basis-set correction procedure and it is by construction more useful for calculating band structures. In addition, we have inspected the difference between the adoption of norm-conserving and ultrasoft potentials in *GW* calculations and found that the norm violation for the *d* shell can lead to less accurate results in particular for charge-transfer systems and late transition metals. A minimal statistical analysis indicates that the correlation of the *GW* data with the density functional theory gap is more robust than the correlation with the experimental gaps; moreover, we identify the static dielectric constant as alternative useful parameter for the approximation of *GW* gap in high-throughput automatic procedures. Finally, we compute the QP band structure and spectra within the random phase approximation and compare the results with available experimental data.

DOI: 10.1103/PhysRevMaterials.2.024601

I. INTRODUCTION

Transition metal oxide (TMO) perovskites are a widely studied class of materials owing to the wide spectrum of interesting physical and chemical properties including colossal magnetoresistance [1,2], metal-insulator transitions [3], superconductivity [4,5], two-dimensional electron gas [6], multiferroicity [7], spin and charge ordering [8], band gaps ranging from the visible to the ultraviolet wavelength [9], as well as chemical and catalytic activity [10]. Many of these fundamental properties have found technological applications in fields as diverse as fuel cells, spintronic, oxide electronics, and thermoelectricity [11]. More recently, oxide perovskites incorporating 4*d* and 5*d* transition metals have attracted increasing attention due to many novel electronic and magnetic quantum states of matter observed in these compounds, originating from spin-orbit-coupling effects. Notable examples are relativistic Mott iridates [12], Lifshitz magnetic insulators [13], and different types of anisotropic magnetic interactions [14–16]. This impressive range of properties and functionalities is the result of two main factors: (i) chemical and structural flexibility and (ii) the occupation and spatial extension of the transition metal *d* orbitals (see Fig. 1). Oxide perovskites can be formed with cations of different sizes, and many different types of lattice and structural distortions can occur depending on the value of the tolerance factor. The specific type of *d* orbitals, instead, modulates the degree of electronic correlation (stronger for localized 3*d* states), electron and spin itinerancy (larger for 5*d*), and spin-orbit-coupling strength (larger for 5*d* orbitals). The strong interplay between lattice, spin, and orbital degrees of freedom leads to a rich structural, electronic, and magnetic phase diagram, characterized by highly tunable phase transitions.

One of the most important quantities of materials in general, and specifically for TMO perovskites, is the band gap, which is essential for the characterization and understanding of the electronic structure and is crucial for virtually all possible practical functionalizations. Experimentally, the optical band gap is measured using spectroscopy techniques such as photoemission, inverse photoemission, x-ray absorption, electron energy loss spectroscopy, to name a few. Spectroscopy experiments can be interpreted and simulated using the Green's function formalism which allows the treatment of excited states beyond the single-particle picture.

Density functional theory (DFT) [17] has been the method of choice for decades to estimate the ground-state properties of many materials. Despite its great success in interpreting

*Corresponding author: cesare.franchini@univie.ac.at

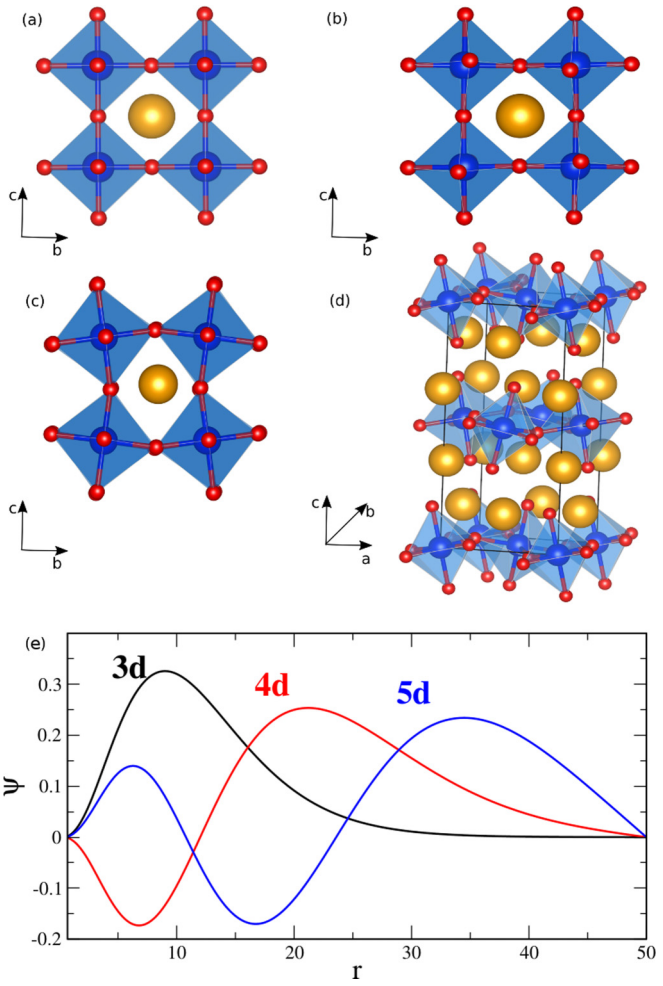

FIG. 1. Different types of lattice distortions (a)–(d) and TM d orbitals (e) in the oxide perovskites studied in this paper. (a) $P_{m\bar{3}m}$ for $SrMO_3$ (M = Sr, Hf, Zr), $SrMnO_3$ and $KTaO_3$; (b) P_{nma} for $LaScO_3$, $LaTiO_3$, $LaCrO_3$, $LaMnO_3$, $LaFeO_3$, $SrTcO_3$, $NaOsO_3$; (c) $P_{21/b}$ for $LaVO_3$; (d) P_{bca} for Ca_2RuO_4. The blue and red balls represent the TM and O ions, respectively. (e) Different degree of spatial extension in $3d$, $4d$, and $5d$ orbitals (derived from atomic calculations).

existing results and predicting experimentally difficult to access properties, DFT is not capable to accurately account for the band gap due to the approximation in treating many-body exchange-correlation effects which hinder the accurate description and calculation of excitation processes [18]. An elegant and increasingly popular method to overcome the limitations of DFT is the GW approximation, originally proposed by Hedin [19]. This method uses single-particle Green's functions and many-body perturbation theory to obtain the excitation spectrum by explicitly computing the self-energy Σ of a many-body system of electrons. This is done by expressing Σ in terms of the single-particle Green's function G and the screened Coulomb interaction W, i.e., $\Sigma = iGW$ [19]. The resulting GW band gaps are much improved compared to the DFT ones and often very close to the measured values [18,20–25].

In GW calculations, it is common to start from DFT orbitals, with which the initial G and W are constructed. There exist different GW schemes depending on the way W and G are updated. The most common choice is the so-called single-shot G_0W_0 starting from DFT orbitals. This usually delivers band gaps in good agreement with experimental measurements [26,27]. The practical disadvantage of the GW method is the large computational cost and memory requirements due to the high number of unoccupied bands [and therefore number of plane-wave (pw) basis functions N_{pw}] required for the accurate calculation of the self-energy and the response function. The convergence of the quasiparticle (QP) energies with respect to the number of basis functions N_{pw} is, therefore, a particularly crucial issue: even for small systems, such as ZnO, over thousand bands are necessary to achieve well-converged results [28,29]. To address this issue, Klimeš *et al.* have recently proposed a finite-basis-set correction scheme [29] based on the formal proof that QP energies converge like $1/N_{\mathrm{pw}}$ [30–32]. Within this scheme, well-converged QP energies extrapolated to the infinite-basis-set limit were obtained for a representative material data set including 24 elemental and binary semiconductors and insulators [29]. Moreover, the authors pointed out the advantage of using norm-conserving (NC) projector augmented wave (PAW) potentials, instead of the commonly employed ultrasoft (US) ones, since US PAWs were found to underestimate the scattering probability from occupied into high-energy unoccupied orbitals [29].

These computational limitations have inhibited the application of GW for larger systems like perovskites, despite some efforts devoted to speeding up GW calculations [33,34]. While there are relatively many GW studies on (non-TMOs) hybrid halide perovskites [35–38], the assessment of GW for TMOs perovskites is scarce [39–45], in particular for $4d$ and $5d$ perovskites [46–48]. The scope of this paper is the calculation of accurate QP energies at the G_0W_0 level for a representative data set of $3d$, $4d$, and $5d$ TMOs perovskites with different types and fillings of the TM d orbitals, different crystal structure and lattice distortions, and different magnetic orderings (see Table I). Specifically, we will consider (1) nonmagnetic (NM) d^0 cubic perovskites: $SrMO_3$ (M= Ti, Hf, Zr) and $KTaO_3$; (2) nonmagnetic and structurally distorted $3d^0$ $LaScO_3$; (3) magnetic d^3 cubic perovskites $SrMnO_3$. Note that to model the G-AFM ordering it is necessary to adapt a supercell containing four formula units; (4) magnetic and structurally distorted systems: (a) $3d$ $LaMO_3$ (M= Ti, V, Cr, Mn, Fe), (b) $4d$ $SrTcO_3$ and Ca_2RuO_4, and (c) $5d$ $NaOsO_3$ (in this case we have included spin-orbit coupling, SOC).

We will inspect and compare two different procedures to compute QP energies and band gaps: (i) In the first scheme the QP energies are not explicitly extrapolated to the infinite-basis-set limit, instead the convergence is inspected with respect to the number of basis functions N_{pw}, the number of $\mathbf{k}$ points, and the total number of bands N [49], and (ii) the basis-set corrected method with QP energies extrapolated to $N_{\mathrm{pw}} \to \infty$.

Also, we will determine a minimal technical setup to achieve sufficiently well-converged values in standard GW calculations without basis-set extrapolation, which we will adopt to compute band structures, obtained by employing Wannier-function fitting of the QP energies (not feasible within the basis-set correction scheme), and optical spectra calculated from the frequency-dependent dielectric tensor. In addition, we will test and discuss the choice of the PAW by comparing US- and NC-based results. As we will see, the convergence rate

TABLE I. Fundamental characteristic of the TMO perovskites data set used in this study. Crystal structures: C = cubic, T = tetragonal, O = orthorombic, M = monoclinic; electronic configuration of the transition metal d shell decomposed over t_{2g} and e_g states; ground-state magnetic ordering: NM = nonmagnetic, and different type of antiferromagnetic (AFM) spin configurations [51,52]. The crystal structures and atomic positions are taken from the following experimental studies: $SrTiO_3$ (Ref. [53]), $SrZrO_3$ (Ref. [54]), $SrHfO_3$ (Ref. [55]), $KTaO_3$ (Ref. [56]), $SrMnO_3$ (Ref. [57]), $LaScO_3$ (Ref. [58]), $LaTiO_3$ (Ref. [59]), $LaVO_3$ (Ref. [60]), $LaCrO_3$ (Ref. [61]), $LaMnO_3$ (Ref. [62]), $LaFeO_3$ (Ref. [63]), $SrTcO_3$ (Ref. [64]), Ca_2RuO_4 (Ref. [65]), $NaOsO_3$ (Ref. [66]). For $SrMnO_3$ we have adopted the calculated lattice constant for the G-type AFM cubic phase, 3.824 Å [57], slightly larger than the corresponding experimental value, 3.80 Å [67].

$SrTMO_3$ (TM= Ti, Zr, Hf)	$KTaO_3$	$LaScO_3$	$SrMnO_3$	$LaTiO_3$	$LaVO_3$	$LaCrO_3$	$LaMnO_3$	$LaFeO_3$	$SrTcO_3$	Ca_2RuO_4	$NaOsO_3$
C-$P_{m\bar{3}m}$	C-$P_{m\bar{3}m}$	O-P_{nma}	C-$P_{m\bar{3}m}$	O-P_{nma}	M-$P_{21/b}$	O-P_{nma}	O-P_{nma}	O-P_{nma}	O-P_{nma}	O-P_{nma}	O-P_{bca}
d^0	d^0	d^0	t_{2g}^3	t_{2g}^1	t_{2g}^2	t_{2g}^3	$t_{2g}^3e_g^1$	$t_{2g}^3e_g^2$	t_{2g}^3	$t_{2g}^3e_g^1$	t_{2g}^3
NM	NM	NM	G-AFM	G-AFM	G-AFM	G-AFM	A-AFM	G-AFM	G-AFM	AFM	G-AFM

is generally highly system dependent, as already pointed out in recent studies [29,49,50], and is largely influenced by the orbital character and by the type of gap.

The paper is organized as follows: The first part is focused on the description of the two convergence procedures and on the computational setup. The main core of this paper is the result section that is divided into three parts dedicated to the analysis of the convergence criteria, to the correlation analysis, and to the discussion of the electronic structure and optical spectra.

II. TECHNICAL AND COMPUTATIONAL DETAILS

The calculations presented in this paper were conducted using the Vienna *ab initio* simulation package (VASP) [68,69] in the framework of the PAW method [70]. The many-body Schrödinger equation was solved within the single-shot G_0W_0 approximation starting from DFT orbitals obtained using the generalized gradient approximation (GGA) parametrization introduced by Perdew, Burke, and Ernzerhof (PBE) [71]. When the GGA was not able to open the gap, a small onsite Hubbard U was added following the scheme of Dudarev [72] ($LaTiO_3$ and $LaVO_3$, $U - J = 2$ eV). The one-particle Green's functions constructed from PBE eigenfunction and the dynamically screened Coulomb interaction W was computed from G_0 within the random phase approximation (RPA). The details of the implementation can be found in Ref. [73]. For the calculation of the polarizability, we have used a discretized frequency grid with about 70 frequency points. This choice should guarantee a reasonably good convergence of the gap with error of the order of ≈50 meV. We have used crystal lattices and atomic positions derived from the experiment (all references are listed in Table I).

The convergence criteria followed to calculate the response function and the correlation part of the self-energy, which requires a summation over many empty states, as well as the dependence of the results with respect to the **k**-point sampling are discussed in the Secs. II A and II B. We have followed and compared two alternative strategies to reach converged results: (i) so-called nonextrapolated method because it does not involve any extrapolation to large $N_{\rm pw}$; we refer to this method as *conventional* since this is the scheme typically used in GW calculations. (ii) The basis-set corrected method which does include an extrapolation of the QP energies to $N_{\rm pw} \to \infty$.

A. Conventional nonextrapolated method

The *conventional* method attempts to converge the QP energies (and therefore the QP energy gap E_g) with respect to a set of three parameters: number of bands (N), energy cutoff for the plane-wave expansion for the orbitals $E_{\rm pw}$ (which determine the total number of plane waves $N_{\rm pw}$), and the number of **k** points. This procedure is schematically shown in Fig. 2. First, E_g is computed as a function of the number of orbitals N for fixed energy cutoff for a given plane-wave expansion (fixed $N_{\rm pw}$) and **k** points [see Fig. 2(a)]. Then, by fixing N and $N_{\rm pw}$ to the optimum values that seemingly guarantee converged results within the required accuracy, E_g is converged with respect to the number of **k** points [see Fig. 2(b)]. This scheme can lead to reasonably well-converged results (as we will see later on); however, it neglects the exceedingly slow convergence of the QP energies with respect to the number of virtual orbitals. Since the conduction band minimum (CBM) and valence band maximum (VBM) converge at about the same rate, errors below 100 meV are often obtained even without explicit extrapolation to the infinite-basis-set limit (this conclusion does not apply to absolute QP energies, i.e., electron affinities and ionicities). Within the conventional method, some fitting procedures for extrapolating the QP energies for $N \to \infty$ have been used in literature [39,43,74]; the exactness of this, however, is not supported by a mathematical proof.

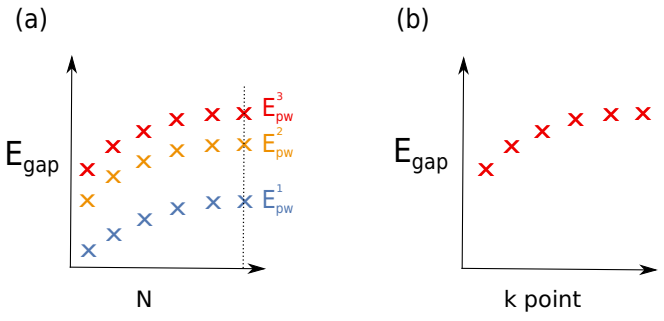

FIG. 2. Schematic representation of the conventional nonextrapolated method. Convergence of the QP energy gap as a function of N and $E_{\rm pw}$. The convergence inspected as a function (a) N (at fixed **k** points and $E_{\rm pw}$) and $E_{\rm pw}$ (for fixed **k** points and N) where $E^3_{\rm pw} > E^2_{\rm pw} > E^1_{\rm pw}$, and (b) shows the convergence of the QP gap with respect to the number of **k** points (for fixed N and $E_{\rm pw}$).

TABLE II. Collection of technical values related to the construction of the US and NC PAWs. Difference $\delta_d = |\psi_d|^2_{\rm AE} - |\psi_d|^2_{\rm US}$ between the all-electron (AE) and pseudized norm of the d partial waves for the $3d$ (Sc, Ti, V, Cr, Mn, and Fe), $4d$ (Zr, Tc, and Ru), and $5d$ (Hf, Ta, and Os) TM ions considered in this study. This value represents the norm violation in the construction of the PAW potentials. The data are extracted from the file FOUROUT, generated by the VASP PAW-generation package. Default energy cutoff for US ($E^{\rm US}_{\rm pw}$) and NC ($E^{\rm NC}_{\rm pw}$) PAWs (in eV), as given in the VASP POTCAR files. Additional details on the employed PAWs are given in the Appendix.

	Sc	Ti	V	Cr	Mn	Fe	Zr	Tc	Ru	Hf	Ta	Os
δ_d	0.13	0.20	0.27	0.33	0.4	0.45	0.02	0.1	0.17	0.03	0.04	0.1
$E^{\rm US}_{\rm pw}$	379	384	384	219	385	388	346	351	348	283	286	319
$E^{\rm NC}_{\rm pw}$	778	785	800	819	781	786	637	639	660	576	584	647

Recently, inspired by similar convergence problems occurring in quantum chemistry calculations [75], Klimeš *et al.* have provided an explicit derivation, that demonstrates that QP energies show a convergence proportional to the inverse of the number of basis functions and introduced finite-basis-set extrapolation method [29]. This is briefly described in the next section. An important difference between these two approaches is that in order to perform a precise extrapolation, it is necessary to work with the complete set of unoccupied orbitals compatible with the given energy cutoff, implying that varying N for a fix energy cutoff as done in the conventional scheme is not a formally correct practice.

B. Basis-set extrapolation

The core aspect of the finite-basis-set correction method derived in Ref. [29] is that the (orbital-dependent) leading-order error of the QP energy decays asymptotically with the inverse of the number of plane waves:

$$\Delta E_m = -\frac{2}{9\pi}\frac{\Omega^2}{N^{\chi}_{\rm pw}}\sum_{\mathbf{g}}\rho_m(\mathbf{g})\rho(-\mathbf{g}). \quad (1)$$

Here, m is the orbital index, $\mathbf{g} = \mathbf{G} - \mathbf{G}'$, where the vectors $\mathbf{G}$ are three-dimensional reciprocal lattice vectors of a cell with volume Ω, ρ and ρ_m are the total and orbital density in reciprocal space, respectively, and $N^{\chi}_{\rm pw}$ is the number of auxiliary basis-set functions used to represent density-related quantities, that is controlled by a plane-wave cutoff $E^{\chi}_{\rm pw}$ [76]. This brings to another important result: both the total number of bands N, the corresponding orbital basis set $N_{\rm pw}$, and the size of the auxiliary basis set $N^{\chi}_{\rm pw}$ need to be increased simultaneously at the same rate, meaning that fixing $E^{\chi}_{\rm pw}$ and converge only with respect to $E_{\rm pw}$ is not a good protocol [29].

In our work we adopt the choice $E^{\chi}_{\rm pw} = 2/3E_{\rm pw}$ and we have used the *complete* basis set for the given $E_{\rm pw}$, meaning that the number of orbitals equals the number of plane waves [76]. $E_{\rm pw}$ was initially set to the maximum plane-wave energy cutoff used to build the element-specific PAWs in the considered material (the values, for US and NC PAWs, are listed in Table II). In practice, we have systematically increased ENCUT until the corresponding total number of plane waves became twice as large as the initial value (corresponding to the default $E_{\rm pw}$).

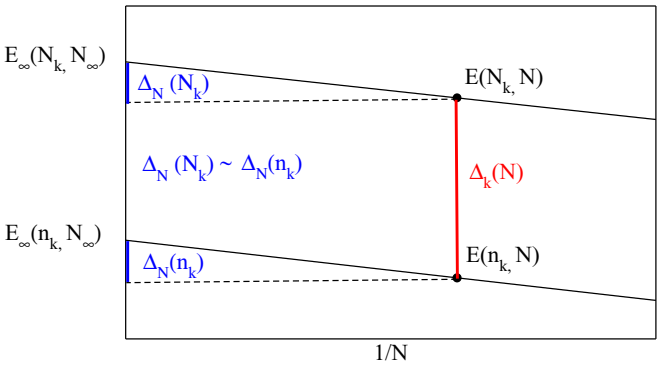

FIG. 3. The schematic representation of the basis-set correction and the **k**-points correction for the QP gap E_g. The labels indicate the contributions in Eq. (2) and are defined in the text.

With Eq. (1) at hand, it is formally possible to extrapolate the results for the QP energies obtained using a finite-basis-set to the infinite-basis-set limit. To reduce the workload, one can take advantage of the fact that the convergence of the QP energies with respect to N depends only weakly on the number of **k** points [29]. Finally, the resulting basis-set correction formula reads as

$$E_\infty(N_k,N_\infty) \approx \underbrace{E_\infty(n_k,N_\infty)}_{\Delta_N(n_k)} \overbrace{- E(n_k,N)}^{\Delta_k(N)} + E(N_k,N), \quad (2)$$

where $E(N_k,N)$ refer to the calculated QP energies with N_k **k** points and N bands, whereas $E(N_k,N_\infty)$ refers to the corresponding extrapolated ($N \to \infty$) QP energies; the variables n_k and N_k indicate the number of **k** points in the small and large **k**-point mesh, respectively. $\Delta_k(N) = E(N_k,N) - E(n_k,N)$ is the **k**-point correction and $\Delta_N(n_k) = E_\infty(n_k,N_\infty) - E(n_k,N)$ the basis-set correction. The graphical interpretation of the basis-set and **k**-point corrections is given in Fig. 3. Owing to the weak **k**-point dependence on the basis-set correction [$\Delta_N(n_k) \approx \Delta_N(N_k)$], in practice it is computationally more convenient to extrapolate Δ_N using few **k** points. Similarly, as $\Delta_k(N)$ is almost independent on N, the **k**-point correction computed for a small N makes the computations less expensive. For the calculations presented in this paper we have used $n_k = 2\times2\times2$ and $N_k = 6\times6\times6$, with some exceptions, specified in the text later on.

C. PAW potentials

By extending the expression of the basis-set correction for the PAW method, Klimeš *et al.* recognized that using US-PAW potentials the correction converges to the wrong value, due to the incompleteness of the partial waves inside the atomic spheres [29]. The authors found that this error becomes smaller if the difference between the norm of the all-electron partial waves and the pseudized partial waves is small, reaching the accuracy of full-potential linearized augmented plane-wave methods [77]. This implies that the choice of the PAW potentials is critical and that the best results are obtained by using NC PAWs, for which the norm is almost fully conserved. As shown in Table II, the deviation

between the all-electron and the pseudized norm, quantified by the difference $\delta_d = |\psi_d|^2_{\rm AE} - |\psi_d|^2_{\rm US}$ between the norm of the all-electron (AE) and US partial waves of the d orbitals, is larger for the more spatially localized $3d$ orbitals and is substantially reduced for more extended and smoother $4d$ and $5d$ orbitals [see also Fig. 1(e)]. Therefore, we expect that the basis-set correction error should be larger for $3d$-based perovskites compared to $4d$ and $5d$ perovskites.

To inspect the influence of the choice of the PAWs on the basis-set correction results we have tested both types of PAWs: US and NC. For the TM ions, we have used *GW* PAWs with the outermost s, p, and d orbitals treated as valence states. The NC-PAW potentials were constructed following the prescription described elsewhere [29].

III. RESULTS AND DISCUSSION

This section presents and discusses the results obtained for the TMOs perovskite data set (see Table I). It is structured in three parts: the first one focuses on the application of the convergence schemes described above to a subset of representative compounds. In the second one, we provide a minimal statistical interpretation of the data obtained and, finally, the third section is dedicated to the calculation of the band structure and optical spectra for all compounds.

A. Convergence tests and extrapolations

In the following, we show the results on the applications of the two convergence schemes, conventional nonextrapolated and basis-set extrapolation, for selected $3d$, $4d$, and $5d$ cases: (i) cubic NM $SrTiO_3$ ($3d$), $SrZrO_3$ ($4d$), and $SrHfO_3$ ($5d$) and (ii) structurally distorted and magnetically ordered $SrMnO_3$ ($3d$), $SrTcO_3$ ($4d$), and $NaOsO_3$ ($5d$). The complete set of results is given in the Supplemental Material (SM) [78].

1. Cubic nonmagnetic systems

We start showing and examining the results for $3d$ $SrTiO_3$, and then we will extend the discussion by including the data for $SrZrO_3$ and $SrHfO_3$. In all these materials, the gap is opened between the filled O-p states at the VBM and empty TM-d states at the CBM.

First, we show the convergence behavior for $SrTiO_3$ using the conventional nonextrapolated scheme by inspecting the variation of the QP indirect gap E^i_g ($R - \Gamma$, highest occupied state at R and the lower unoccupied state at Γ) as a function of N, $E_{\rm pw}$, and the number of **k** points, using both US and NC PAWs. Similar results and conclusions are obtained for QP energies, but since we are primarily interested in the behavior of the band gap, the discussion and analysis will be focused on the direct and indirect band gap (i.e., differences of QP energies).

The results are displayed in Fig. 4. From Fig. 4(a) we note that using US PAWs the results are largely sensitive on N, and to a lesser extent on $E_{\rm pw}$, and well-converged values are achieved for $N \approx 1500$ and $E_{\rm pw} \approx 600$ eV. By employing NC PAW, the convergence with respect to N is much faster, $N \approx 1000$, and is sufficient to obtain the same level of accuracy obtained at US level (as we will see below, the faster convergence using NC PAWs is in this case related to

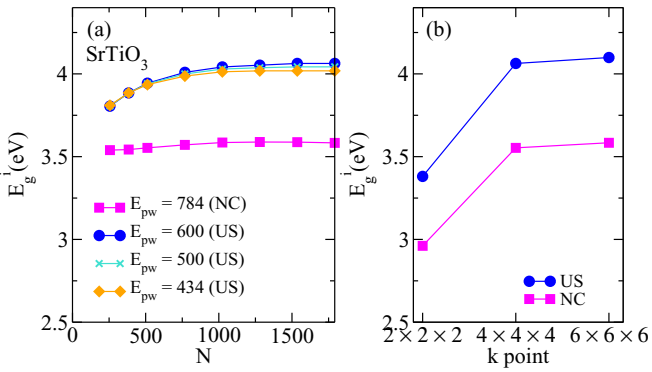

FIG. 4. Conventional nonextrapolated method applied to $SrTiO_3$. Convergence of the indirect QP band gap E^i_g of $SrTiO_3$ with respect to (a) number of bands N and plane-wave cutoff energy $E_{\rm pw}$ (**k**-point mesh fixed to $4 \times 4 \times 4$), and (b) size of the **k**-point mesh for N and $E_{\rm pw}$ fixed to the optimum values for US and NC potentials.

similar convergence rates for CBM and VBM for NC PAWs). However, owing to the generally larger default energy cutoffs for NC PAWs (see Table II), it is computationally prohibitive to scan higher values of the cutoff energy. The dependence of E^i_g on the number of **k** points, displayed in Fig. 4(b), shows that a $4 \times 4 \times 4$ grid is sufficient to achieve an accuracy of about 0.03 eV.

The final values of the US and NC indirect band gaps E^i_g, 4.06 eV (almost identical to the one reported in Ref. [43] using the same scheme) and 3.55 eV, respectively, differ by about 0.5 eV and are both larger than the measured value 3.3 eV [79] (see Table III). The difference between the US PAWs and NC PAWs is due to the relatively large norm violation for the Ti US PAW, 0.2, which causes a quite different QP shift of the empty d states at the bottom of the conduction band in US- and NC-based calculations (0.68 eV, see Table III). On the other side, the difference in the QP shift between NC and US calculations is substantially smaller for the top of the valence band, mostly populated by O-p state (0.11 eV, see Table III). This issue will be further discussed in the context of the data obtained using the basis-set extrapolation, at the end of this subsection.

The basis-set extrapolation data for $SrTiO_3$ are collected in Fig. 5, where we show the evolution of E^i_g and the **k**-point corrections upon N, as well as the basis-set correction Δ_N as a function of the size of the **k**-point mesh. We highlight once more that here $N_{\rm pw}$ refers to the maximum number of plane waves compatible to a given plane-wave cutoff energy $E_{\rm pw}$. In this case ($SrTiO_3$), we have gradually increased N from 1200 to about 2500 using US PAWs ($E_{\rm pw} = 434$ eV), and from 3000 to 6000 using NC PAWs (the minimally required $E_{\rm pw}$ is significantly larger for the NC PAWs, 785 eV, which leads to a much larger number of basis functions). We have also inspected the convergence for three different **k**-point meshes: $2 \times 2 \times 2$, $4 \times 4 \times 4$, and $6 \times 6 \times 6$. The curves plotted in Figs. 5(a) and 5(d) clearly indicate that E^i_g converges linearly with respect to $1/N$ for both types of PAWs. The values of E^i_g, in particular its $N \to \infty$ extrapolation, vary with the number of **k** points but the **k**-point correction Δ_k (≈600 meV) depends only marginally on N [see Figs. 5(b) and 5(e) and

TABLE III. Collection of data related to the convergence tests for selected $3d$, $4d$, and $5d$ perovskites (cubic-NM and distorted-AFM, see text). Energy differences between the US and NC QP energies at the CBM and VBM at Γ $\Delta E^V_{\rm QP} = |E^{\rm NC}_{\rm QP\text{-}VBM} - E^{\rm US}_{\rm QP\text{-}VBM}|$ and $\Delta E^C_{\rm QP} = |E^{\rm NC}_{\rm QP\text{-}CBM} - E^{\rm US}_{\rm QP\text{-}CBM}|$, the norm violation δ_d (same as in Table II), the nonextrapolated (nE) and extrapolated (E) values of the indirect band gap E^i_g, the basis-set correction Δ_N and the **k**-point correction Δ_k [evaluated with a reduced number of **k** points $n_k = 2 \times 2 \times 2$ and $N \approx 400$–500, respectively, and $N_k = 6 \times 6 \times 6$, see Eq. (2)]. E^i_g, Δ_N, and Δ_k are provided for both type of PAWs (US and NC). Within the conventional method, we have used NC PAW only for the representative case of $SrTiO_3$. For non-d^0 compounds $SrMnO_3$, $SrTcO_3$, $NaOsO_3$ (with SOC), the amount of d character in the valence (d_V) and conduction (d_C) band is also given. Available experimental data for the gap are also listed. All energies are given in eV.

						Δ_N		Δ_k		E^i_g				
										US	NC	US	NC	
Compound	$\Delta E^V_{\rm QP}$	$\Delta E^C_{\rm QP}$	δ_d	d_V	d_C	US	NC	US	NC	(nE)	(nE)	(E)	(E)	$E^{\rm expt}_g$
$SrTiO_3$	0.11	0.68	0.20			0.20	0.01	0.56	0.59	4.08	3.55	4.06	3.55	3.3 [79–81]
$SrZrO_3$	0.11	0.04	0.02			0.14	0.18	0.36	0.36	5.29		5.36	5.43	5.6 [82]
$SrHfO_3$	0.10	0.09	0.03			0.19	0.12	0.34	0.36	5.69		5.76	5.81	6.1 [46]
$SrMnO_3$	0.27	0.43	0.4	0.54	0.93	0.03	−0.03	0.23	0.31	1.75		1.66	1.46	
$SrTcO_3$	0.30	0.33	0.1	0.86	0.87	0.01	0.02	−0.13	−0.14	1.14		1.18	1.20	
$NaOsO_3$	0.26	0.27	0.1	0.73	0.78	0.03	0.01	−0.23	−0.26	0.27		0.28	0.27	0.1 [83]

Table III]. This represents one of the great advantages of the extrapolation scheme: Δ_k can be determined using a small N (the default value), thereby reducing the computational cost of the calculation. Moreover, Δ_k does not depend on the type of PAW potential used but it is sensitive to the specific **k** point at which the QP energy correction is calculated: for E^i_g Δ_k is 600 meV, but the corresponding correction for the direct gap at Γ, E^Γ_g (Γ − Γ gap) is reduced by about 100 meV (similar observations were made in Ref. [29] for most materials, specifically AlAs and GaAs). A further positive aspect of this scheme is that the basis-set correction Δ_N does not vary much with respect to the size of the **k**-point mesh [Figs. 5(c) and 5(f)]: Δ_N can be evaluated using a small **k**-point mesh, typically $2 \times 2 \times 2$, which also helps in decreasing the CPU time. However, unlike Δ_k, which is essentially insensitive to the choice of the potential, Δ_N is one order of magnitude smaller for NC-PP (0.01 eV against 0.2 eV, see Table III). Also, the NC value of the fundamental gap, 3.55 eV (the same for both the conventional and the extrapolated methods), is in better agreement with the measured value, 3.3 eV, as compared to the US gaps, which are substantially larger (3.94 and 4.08 eV, see Table III). The reason for the improved description of $SrTiO_3$ is the improved treatment of the $3d$ CBM states, which show a larger slope with the NC potentials (Fig. 6).

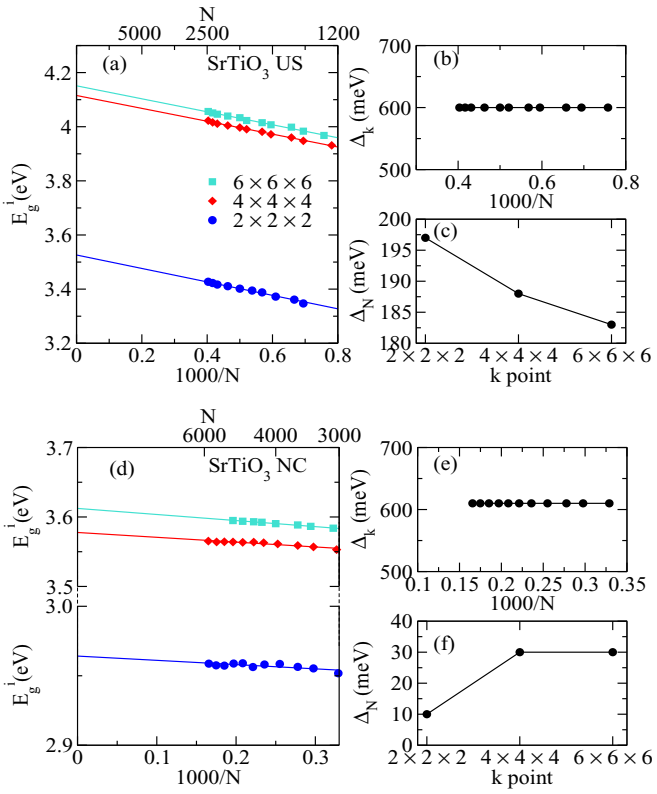

FIG. 5. Basis-set correction data for $SrTiO_3$ using US (a)–(c) and NC (d)–(f) PAWs. For each type of PAW three different graphs are shown: (a), (d) convergence of the QP band gap E^i_g with respect to the inverse of the number of bands ($1000/N$); (b), (e) **k**-point correction Δ_k as a function of $1000/N$; (c), (f) basis-set correction Δ_N as a function of **k** points.

The convergence tests for the other two members of the cubic-NM $3d$-$4d$-$5d$ series, $SrZrO_3$ and $SrHfO_3$, are displayed in Fig. 6 where we report the dependence of E^i_g on the number of bands N as well as the evolution of the QP corrections to the Kohn-Sham DFT eigenvalues at Γ for the conduction band minimum (CBM, TM-d^0) and valence band maximum (VBM, O-p). For the sake of comparison, the corresponding data for $SrTiO_3$ are also included. As a general result, we found that by applying Eq. (2), well-converged values of E_g [$E_g(N_k, N_\infty)$] are obtained by setting $n_k = 2 \times 2 \times 2$, $N_k = 6 \times 6 \times 6$ (but also $N_k = 4 \times 4 \times 4$ leads to accurate results); these data are reported in Table III.

The most important result that one notices is that the difference between NC and US data is substantially reduced for $SrZrO_3$ and $SrHfO_3$, as compared to $SrTiO_3$ (see Fig. 6, and note the different scale for E^i_g plots). As already mentioned, the difference in Δ_N between NC and US energies in $SrTiO_3$ is about 0.5 eV, whereas for $SrZrO_3$ and $SrHfO_3$ it is almost zero: US and NC PAWs deliver roughly the same Δ_N for both materials, ≈0.15 eV (see Table III). This result can be

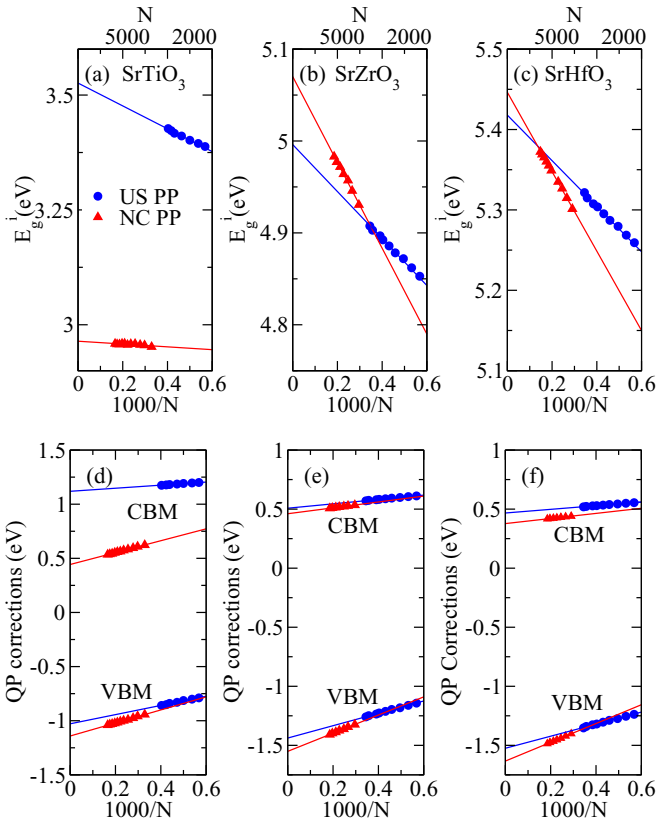

FIG. 6. E_g^i and QP corrections to Kohn-Sham eigenvalues ($E^{\mathrm{QP}} - E^{\mathrm{KS}}$) for the CBM and VBM at Γ as a function of $N = N_{\mathrm{pw}}$ for $SrTiO_3$ (a), (d), $SrZrO_3$ (b), (e), and $SrHfO_3$ (c), (f), computed within the basis-set correction scheme using a $2 \times 2 \times 2$ **k**-point mesh.

readily explained by the much lower norm violation δ_d in 4*d* Zr (0.02) and 5*d* Hf (0.03) as compared to 3*d* Ti (0.2), which originates from the smoothness of the 4*d* and 5*d* orbitals as compared to the more localized nature of 3*d* orbitals (see Fig. 1). This conclusion correlates well with the behavior of the QP corrections shown in Fig. 6, in particular, by looking at the differences between the US and NC QP corrections at the CBM and VBM at Γ, defined as $\Delta E^V_{\mathrm{QP}} = |E^{\mathrm{NC}}_{\mathrm{QP\text{-}VBM}} - E^{\mathrm{US}}_{\mathrm{QP\text{-}VBM}}|$ and $\Delta E^C_{\mathrm{QP}} = |E^{\mathrm{NC}}_{\mathrm{QP\text{-}CBM}} - E^{\mathrm{US}}_{\mathrm{QP\text{-}CBM}}|$: for the Ti-3*d* empty states ΔE^C_{QP} is 0.68 eV, whereas for Zr and Hf d^0 states as well as for the highest occupied O-*p* states ΔE^C_{QP} and ΔE^V_{QP} are in the range 0.04–0.1 eV. The exact values are listed in Table III.

In terms of band gaps, US and NC PAWs lead to similar values, in particular for 5*d* $SrHfO_3$ (5.36 and 5.43 eV, respectively) in satisfactory agreement with the available experimental estimates (see Table III).

To conclude this part, we have shown that the type of convergence scheme, the type of potential employed in the calculations, and the type of TM *d* orbital affect the QP energies and therefore the final "converged" value of the band gap. Overall, we have tested four different procedures to compute the gap: conventional scheme (no extrapolation, labeled "nE" in Table III) and basis-set extrapolation (labeled "E") using US or NC PAWs. As mentioned before, nE-NC calculations were only done for $SrTiO_3$. The main conclusion is that extrapolated NC values agree better with the experimentally measured data, in particular for 3*d* $SrTiO_3$ for which the large norm violation underestimates the electronic correlation contribution to the Ti 3*d* CBM states for the US-PAW potentials, and thus a too large band gap [29]. For 4*d* $SrZrO_3$ and 5*d* $SrHfO_3$ the difference between NC and US PAWs is strongly attenuated and the final extrapolated values of the gap are almost identical. Also, our results suggest that there are not pronounced differences in the gap between the two schemes for a specific type of potential: the two schemes yield very similar gaps for $SrTiO_3$, 3.55 eV (see Table III). Qualitatively similar results are obtained for the larger and magnetically ordered 3*d*, 4*d*, and 5*d* systems, as discussed below.

2. *Large magnetic systems*

We show here the convergence tests for the basis-set extrapolation scheme applied to the t_{2g}^3 series $SrMnO_3$, $SrTcO_3$, and $NaOsO_3$. For the other compounds included in our data set as well as for the data obtained using the conventional scheme, we will only discuss the converged values of the gap and compare them to available experimental measurements. Further details and graphs can be found in the Supplemental Material (SM) [78] and in Ref. [84].

The unit cells used to model $SrMnO_3$, $SrTcO_3$, and $NaOsO_3$ contain four formula units (20 atoms), which are necessary to model the internal structural distortions and the antiferromagnetic ordering (see Table I). This leads to an increase of the number of basis functions and, therefore, to more substantial memory requirements and computing times. As a result, the calculations become technically heavier and almost prohibitive for NC-based calculations. Due to this computational limitation, in some cases, we have performed the NC-based extrapolation using only 2 or 3 points (see Fig. 7 and SM).

The trends for the QP energies and gaps for this series are plotted in Fig. 7. For US-PAW calculations we have inspected the N range from ∼5000 up to ∼10 000 in about 10 steps (a denser mesh has been used for the largest N in order to improve the extrapolation for $N \to \infty$); however, for NC calculations due to the computational restrictions mentioned above, we could scrutinize a smaller N range, between 10 000 and 12 000.

The violation of the norm is much larger for 3*d* Mn (0.4) compared to 4*d* Tc and 5*d* Os (0.1), which explains the bigger difference between NC and US results in $SrMnO_3$ as compared to $SrTcO_3$ and $NaOsO_3$, particularly evident for the QP correction in Fig. 7(d) but also the gap [Fig. 7(a)]. Unlike d^0 cubic perovskites, for this t_{2g}^3 series the difference between NC and US PAW is not limited to the bottom of the conduction band, but is also manifested at the top of the valence band that has a strong *d* character. This is shown in the bottom panels of Fig. 7, that displays the QP corrections at the US and NC levels for the VBM and CBM. The energy shifts ΔE^V_{QP} and ΔE^C_{QP} that measure the differences between the US and NC QP corrections at the CBM and VBM tabulated in Table III show that in $SrMnO_3$ the difference is larger for the CBM than VBM (0.43 and 0.27 eV, respectively), whereas in $SrTcO_3$ and $NaOsO_3$ the deviation is about the same for filled and empty states, ≈0.3 eV. This behavior can be explained by the amount of *d* states present in the CBM and VBM, which is also listed in Table III (see the additional column for $SrMnO_3$, $SrTcO_3$, and

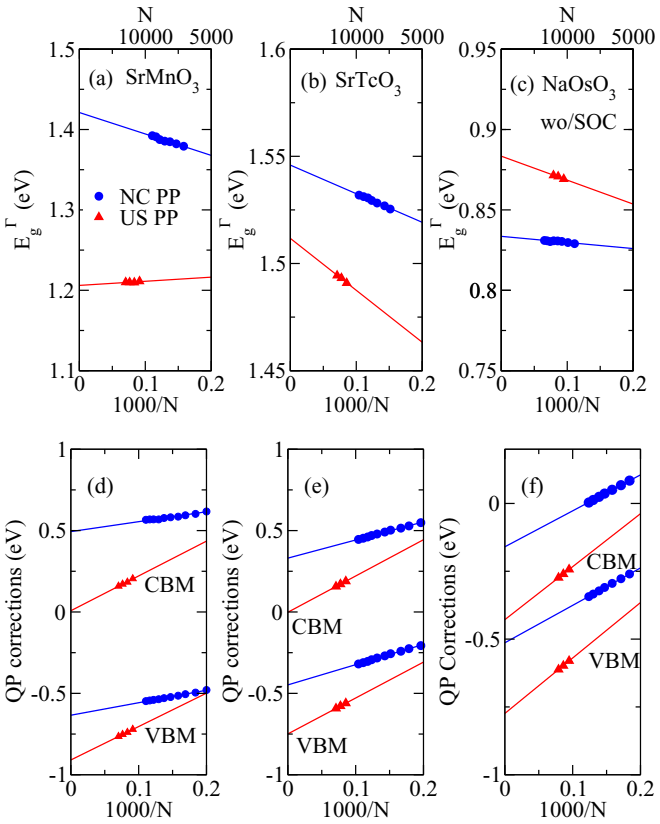

FIG. 7. Band gap E_g^Γ and QP correction $E^{QP} - E^{KS}$; similar to Fig. 6 but for $SrMnO_3$, $SrTcO_3$, and $NaOsO_3$ [without (wo) SOC].

$NaOsO_3$): in $SrTcO_3$ and $NaOsO_3$, the CBM and VBM possess about the same amount of d character, ≈0.8, but in $SrMnO_3$ the CBM is almost completely formed by Mn-d states, 93%, twice larger than the d population at the valence band, 54%.

As expected from the above considerations, the final values of the extrapolated gap for this subseries vary less than for Sr(Ti, Zr, Hf)O_3. For $SrMnO_3$, the NC potential lowers the gap by 0.2 eV, for the other materials there is hardly any difference between the predicted gaps. This outcome is qualitatively similar to the situation discussed for the 3d, 4d, and 5d cubic nonmagnetic perovskites (see Table III).

The complete collection of band gaps for the entire series of perovskites considered in our study is compiled in Table IV. A graphical summary of the comparison between the computed (GW and DFT) and available photoemission and inverse photoemission spectroscopy measurements is provided in Fig. 8. The technical parameters (energy cutoff, number of **k** points, and number of bands N) that guarantee well-converged QP energies (accuracy ≈100 meV) within the conventional nonextrapolated scheme are listed in Table V.

Clearly, GW outperforms DFT, which underestimates the gaps by more than 50% and, in some cases ($NaOsO_3$, $LaTiO_3$, and $LaVO_3$), finds a metallic solution. This is a well-known behavior that has been widely discussed in literature [18,22–25,40]. Regardless of the specific convergence scheme and type of potential, the GW gaps are in overall good agreement with experiment. However, we should note that the experimental data must be treated with care because perovskite materials can often exhibit oxygen deficiencies that unavoidably alter

TABLE IV. Compilation of the calculated (G_0W_0) and experimental band gaps for the perovskite data set studied in this paper for both types of convergence schemes (extrapolated E and nonextrapolated nE) using US- and, when available, NC-based data. Both the calculated direct gap at Γ (E_g^Γ) and the indirect gap (E_g^i, only if smaller than E_g^Γ) are listed. As explained in the text NC-nE results are only given for $SrTiO_3$. The results are also compared with other previously calculated GW results. For $NaOsO_3$ the calculations were done including SOC. Due to the large computational cost, it was not possible to obtain NC data for Ca_2RuO_4. The experimental techniques used to extract the gap are also reported: photoemission spectroscopy (Refs. [79,80,85]), electron energy loss spectroscopy (Ref. [81]), optical spectroscopy (Refs. [9,46,82]), spectroscopic ellipsometry (Ref. [86]), x-ray absorption spectroscopy (Ref. [87]), and optical conductivity (Ref. [83]). All energies are expressed in eV.

		E_g^Γ		E_g^i			
Compound	PAW	(E)	(nE)	(E)	(nE)	E_g^{expt}	Other GW
$SrTiO_3$	US	4.45	4.39	4.08	4.06	3.3 [79–81]	3.82 [39,43]
	NC	3.94	3.99	3.55	3.55		
$SrZrO_3$	US	5.73	5.64	5.36	5.29	5.6 [82]	
	NC	5.80		5.43			
$SrHfO_3$	US	6.17	6.01	5.76	5.69	6.1 [46]	
	NC	6.21		5.81			
$KTaO_3$	US	4.40	4.31	3.67	3.59	3.6 [86]	3.57 [46] 3.51 [88]
	NC	4.39		3.64			
$LaScO_3$	US	4.87	4.56			6.0 [9]	
	NC	4.93					
$LaTiO_3$	US	1.12	1.00	0.63	0.49	0.1 [9]	0.77 [40]
	NC	1.17		0.54			
$LaVO_3$	US	1.73	1.74	1.19	1.14	1.1 [9]	2.47 [40]
	NC	1.71		1.14			
$LaCrO_3$	US	2.98	2.95			3.3 [9]	3.25 [40]
	NC	2.77					
$LaMnO_3$	US	1.33	1.34	0.96	0.97	1.1 [9]	1.63 [40]
	NC	1.30		0.87			
$LaFeO_3$	US	2.61	2.65	1.95	1.91	2.1 [9]	1.76 [40]
	NC	2.46		1.73			
$SrMnO_3$	US	1.66	1.75				
	NC	1.46					
$SrTcO_3$	US	1.62	1.62	1.18	1.14		
	NC	1.58		1.20			
Ca_2RuO_4	US	0.96	0.98	0.53	0.50	0.3-0.5 [87]	
$NaOsO_3$	US	0.79	0.82	0.28	0.27	0.1 [83]	
	NC	0.92		0.27			

the value of the gap. In addition to this, we should also mention that the GW gap refers to the fundamental gap, meaning that excitonic effects are not taken into account. The calculation and the experimental estimation of electron-hole interactions are not an easy task [18,89] and remain a largely unexplored issue in TM perovskites.

US and NC data are generally very similar, apart from the 3d systems, in particular, titanates $SrTiO_3$ and $LaTiO_3$, for which the US gaps are larger by about 15% compared to the NC values and, to a lesser extent, $LaCrO_3$, $LaFeO_3$, $LaMnO_3$ where the difference reduces to ≈10%: clearly, the discrepancy is correlated with the difference δ_d between the all-electron and pseudized norm of the 3d orbitals, which is

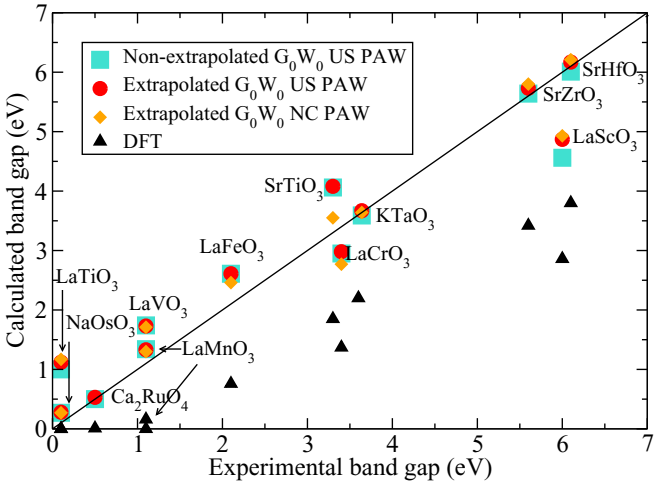

FIG. 8. Comparison between the DFT and G_0W_0 band gaps and available experimental measurements (reference given in Table IV). The G_0W_0 refer to three different sets: nonextrapolated results obtained using US potentials, and basis-set corrected values using both type of potentials, US and NC (not for Ca_2RuO_4).

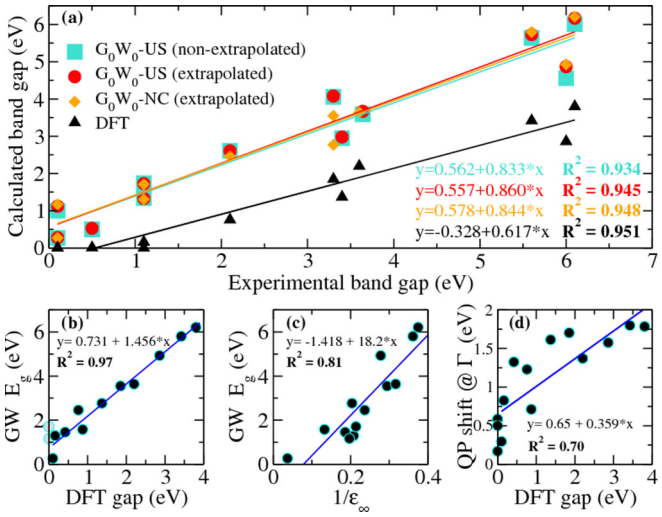

FIG. 9. Statistical interpretation of the *GW* data by means of a linear regression. (a) Comparison between the calculated and experimental gaps. The calculated values include G_0W_0 results obtained following the different schemes discussed in the main text: conventional nonextrapolated scheme using US PAW and the basis-set correction procedure using both NC and US PAW. (b) Correlation between the G_0W_0 and the DFT gap. (c) Correlation between the G_0W_0 gap and the calculated static dielectric constant ϵ_∞. (d) Comparison between the DFT gap and the QP shift at Γ. In each panel, the linear relation and the R^2 factors are given in the insets.

larger for *d* elements (as discussed previously, see Table II), and the character of the VBM and CBM. Finally, the comparison between extrapolated and nonextrapolated schemes (here inspected for US PAW only) confirms that these two methods lead to similar results for the entire TM perovskite data set, with differences of about 0.1 eV. The only exception is $LaScO_3$ for which the nonextrapolated value of the gap is 0.3 eV smaller than the extrapolated one. We reaffirm, however, that only the basis-set corrected scheme is founded on a solid mathematical basis. Especially for US PAWs, it is also computationally more efficient than the nonextrapolated scheme as it reduces the number of calculations to be performed with a large number of bands and **k** points.

TABLE V. Set of parameters (energy cutoff E_{pw}, **k**-point mesh, and number of bands N) used for the calculation of the band structures and optical spectra at G_0W_0 level within the nonextrapolated scheme. This setup guarantees well-converged QP energies within a accuracy of typically 100 meV. All of the parameters are for US PAWs except for $SrTiO_3$ where NC PAW is used.

Compound	E_{pw}	**k**-point mesh	N
$SrTiO_3$	600	4 × 4 × 4	512
$SrZrO_3$	650	4 × 4 × 4	1791
$SrHfO_3$	650	4 × 4 × 4	2304
$KTaO_3$	500	4 × 4 × 4	896
$SrMnO_3$	500	4 × 4 × 2	400
$SrTcO_3$	500	5 × 3 × 5	512
Ca_2RuO_4	500	4 × 4 × 2	512
$NaOsO_3$	500	5 × 3 × 5	400
$LaScO_3$	500	5 × 5 × 3	1280
$LaTiO_3$	500	5 × 3 × 5	400
$LaVO_3$	500	5 × 3 × 5	400
$LaCrO_3$	500	5 × 3 × 5	400
$LaMnO_3$	500	5 × 3 × 5	400
$LaFeO_3$	500	5 × 3 × 5	400

B. Statistical correlations

Even though the material data set under scrutiny is limited to 14 compounds, a minimal statistical analysis of the results is useful, in particular considering the complexity of the systems, the degree of accuracy of the method adopted, and the increasing interest in automatizing first-principles calculations within a high-throughput framework [90]. To this end, we have inspected possible correlations between different types of identifiers: QP gap, QP shift, DFT gap, and the static dielectric constant ϵ_∞. The results are summarized in Fig. 9. First, we note that there is a relatively strong correlation, ∼0.97, between the calculated and experimental gaps, regardless of the specific *GW* flavor (NC-PAW extrapolated data are slightly better than the others) and the correlation is essentially identical for *GW* and DFT [see Fig. 9(a)]. This result is in line with the very recent results of van Setten and co-workers [49], who found a correlation of $R^2 = 0.962$ (*GW*) and 0.957 (DFT) for a larger set of 77 materials including monoatomic and binary semiconductors. In the insets of Fig. 9(a) we provide the linear relations to reproduce the experimental gap starting from the calculated band gaps.

In agreement with the conclusions of Ref. [49] we confirm that also for TMO perovskites the correlation between the *GW* and DFT gap, 0.97, [see Fig. 9(b)] is larger than the correlation between the calculated and experimental gap [see Fig. 9(a)], meaning that it is more accurate (smaller average error) to reproduce the *GW* gap starting from PBE gap than to approximate the experimental gap based on *GW* data. A standard linear regression procedure leads to an $E_g^{GW} = 0.731 + 1.456 E_g^{DFT}$ relation, which should be compared with

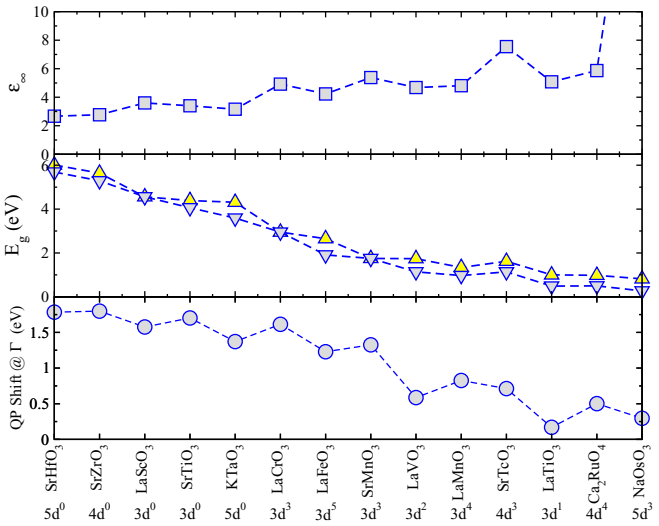

FIG. 10. Comparison between calculated QP shift, band gap (indirect, down triangles, and direct at Γ, up triangles), and average of the diagonal component of the static dielectric tensor using the conventional nonextrapolated scheme and adopting US PAWs. The QP shift is defined as the difference between the G_0W_0 QP energy and DFT eigenvalue.

the corresponding relation found by van Setten, namely, $E_g^{GW} = 0.51 + 1.32E_g^{\mathrm{DFT}}$ [49].

Interestingly, we found that the static dielectric constant ϵ_∞ (the average of the diagonal part of the static dielectric tensor, see next section for more details) is another identifier that can be used in high-throughput automatic GW calculations. In this case, the correlation between the G_0W_0 gap and ϵ_∞ is quantified by the relation $E_g^{GW} = -1.418 + 18.2\frac{1}{\epsilon_\infty}$, with an associated correlation of 0.81 [see Fig. 9(c)]. Even though the linear relation between the GW gap and ϵ_∞ can be useful, the accurate calculation or measurement of ϵ_∞ is not an easy task [27,91]. Finally, we have also inspected the relation between the DFT gap and the QP shift @ Γ but we found a rather low correlation of 0.70 [see Fig. 9(d)].

To conclude this part, we collect in Fig. 10 the various identifiers used for the statistical analysis: band gap, QP shift, and ϵ_∞. The cubic d^0 compounds exhibit the largest gaps (4–6 eV) and the largest QP shifts (≈1.5 eV). In the 3d series, the gap E_g^Γ decreases progressively depending on the filling of the d orbitals (larger, 1.7–3 eV, for half-filled systems) and so does the QP shift (1.5–0.6 eV). Finally, for 4d and 5d compounds with partially filled d bands the direct gap at Γ is ≈1 eV, and the corresponding QP shift is about 0.5 eV. Summing up, for less correlated d^0 and 4-5d materials the QP shift is roughly 25% of the direct gap, whereas in the more correlated 3d perovskites the QP shift increases to 50%–60% of the gap. As expected, the dielectric constant follows an opposite trend. It increases with decreasing gap size and approaches a metalliclike limit for $NaOsO_3$ (which is on the verge of a Lifshitz insulator-to-metal transition [13]) for which $\epsilon_\infty \approx 27$.

C. Band structures and optical spectra

After having analyzed in detail the convergence of the QP energies in the G_0W_0 method, we turn now to the calculation of the electronic band structure and optical spectra for the considered TM perovskite data set. To this end, we have used US PAWs and the nonextrapolated scheme according to the technical setup given in Table V. In fact, for the calculation of the band structure, the basis-set correction scheme is unpractical because it would be necessary to apply the extrapolation procedure to each QP energy using a sufficiently large **k**-point mesh (required for the Wannier interpolation, see below). This would clearly result in a cumbersome procedure, and the need to use many **k** points would wipe out the advantages of the **k**-point correction scheme.

Due to technical reasons related to the **k**-point sampling, it is presently not possible to calculate the QP energies for nonuniform **k**-point meshes in the GW method. A common alternative is the interpolation of the QP energies obtained for a uniform mesh using maximally localized Wannier functions (MLWF); in VASP this is done by using the VASP2WANNIER90 interface [42] which connects VASP with the WANNIER90 suite [92]. We have followed this approach for the calculation of the band structures, and used as an orbital basis for the Wannier projections the full d manifold of the TM ion (e_g and t_{2g}) and the O-p states. This choice is adequate to accurately describe the electronic bands in a few eV windows around the Fermi energy, as for all materials the top part of the valence band has mixed O-p/TM-d character and the bottom portion of the conduction band is generally dominated by empty TM-d states (see SM [78]).

The band structures are compiled in Fig. 11, where we show a comparison between PBE and GW-derived bands, along with the computed GW density of states (DOS). First, we note that the quality of the Wannier interpolation is generally very good, as established by the excellent match between the interpolated bands and the actual GW QP energies used for the interpolation procedure (shown as filled circles) and by the smoothness of the electron dispersions.

By combining the information included in the band structures and DOS with the quantitative analysis of the orbital character at the CBM and VBM at the Γ point (see Table VI) it is possible to draw some conclusions on the type of band gap. The d^0 cubic systems $SrTiO_3$, $SrZrO_3$, $SrHfO_3$, and $KTaO_3$ are band insulators characterized by a p-d fundamental gap that is also well visible as first excitation peak in the calculated and experimental optical spectra shown in Fig. 12. Also, $LaScO_3$ falls in the category of band insulators, even though the conduction band has a sizable amount of O-p states, which causes a broadening of the first excitation peak (see Fig. 12). The other compounds have a predominant d-d fundamental gap, with some distinctions: $LaTiO_3$ exhibits a clear Mott gap with only marginal (about 10%) O-p states at the valence band; $LaVO_3$, $LaCrO_3$, $LaMnO_3$, and $SrTcO_3$ appear to have a predominant Mott character too, but it is known that the gap in $LaMnO_3$ originates also from the Jahn-Teller instability [97,98]; $SrTcO_3$ was reported to possess a substantial itinerant character, which places it on the verge of a Mott transition [99,100]. The data suggest that $SrMnO_3$ and $LaFeO_3$ can be assimilated to an intermediate Mott/charge-transfer nature, as they have a strong intermix of O-p and TM-d states at the valence bands, while the conduction bands are largely formed by empty d orbitals. Ca_2RuO_4 exhibits a pd-pd gap, with 25% of O-p states at both VBM and CBM. $NaOsO_3$ is a

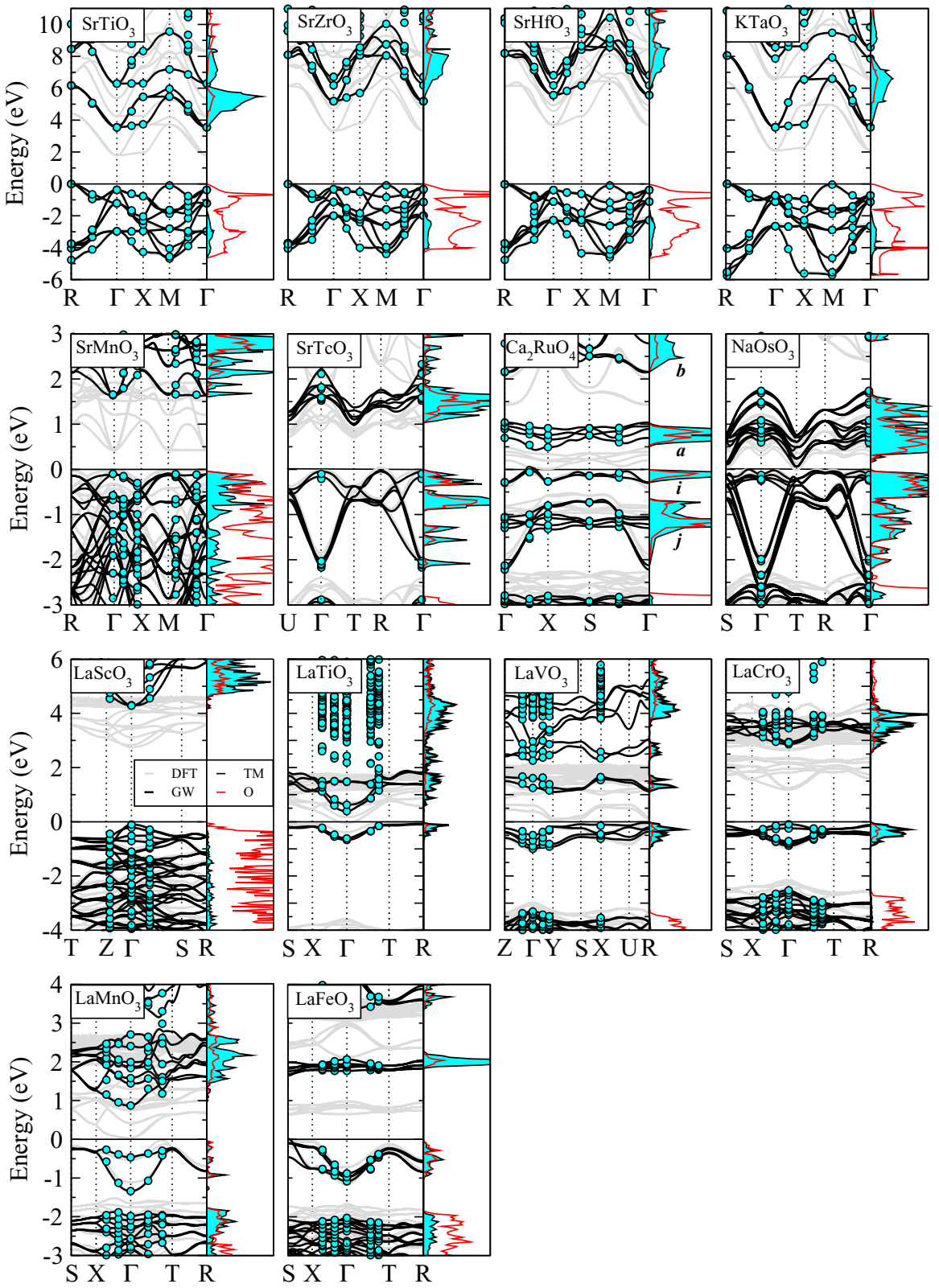

FIG. 11. Collection of the calculated band structures for DFT (gray lines) and *GW* (black) together with the *GW* density of TM-*d* (shadow, cyan line) and O-*p* (full line, red) states. The filled circles indicate the calculated *GW* QP energies (used for the Wannier interpolation). As mentioned in the main text, the DFT calculations for $LaTiO_3$ and $LaVO_3$ were performed with the addition of a small effective U.

TABLE VI. Percentage of O-p and TM-d states at Γ at the VBM and CBM from the projected orbitals. For Ca_2RuO_4, the data in brackets refer to the values taken for the VBM and CBM at (0.25,0,0).

Compound	VBM O-p	VBM TM-d	CBM O-p	CBM TM-d
$SrTiO_3$	100 %	0 %	0 %	100 %
$SrZrO_3$	100 %	0 %	0 %	100 %
$SrHfO_3$	100 %	0 %	0 %	100 %
$KTaO_3$	100 %	0 %	0 %	100 %
$SrMnO_3$	45 %	54 %	3 %	93 %
$LaScO_3$	98 %	1 %	8 %	76 %
$LaTiO_3$	6 %	90 %	2 %	93 %
$LaVO_3$	10 %	89 %	14 %	81 %
$LaCrO_3$	20 %	78 %	4 %	92 %
$LaMnO_3$	24 %	72 %	11 %	85 %
$LaFeO_3$	33 %	61 %	7 %	90 %
$SrTcO_3$	14 %	86 %	13 %	87 %
Ca_2RuO_4	14 %	84 %	24 %	74 %
	(24 %)	(75 %)	(24 %)	(75 %)
$NaOsO_3$	23 %	73 %	18 %	78 %

peculiar case, characterized by electron and spin itinerancy, a relatively strong SOC, and a weak electron-electron correlation [13,83,101]. In this case, the valence and conduction bands are formed by a strong mixture of O-p and Os-d states.

Finally, we used the GW QP energies to calculate the dielecric function in the independent particle approximation. The real (ϵ_1) and imaginary (ϵ_2) parts of dielectric functions $\epsilon = \epsilon_1 + i\epsilon_2$ (shown in Fig. 13) were used to compute the optical conductivity spectra as

$$\sigma(\omega) = -i\omega\epsilon_0[\epsilon(\omega) - 1], \tag{3}$$

where ε_0 is the vacuum dielectric constant. The results are displayed in Fig. 12 and include a comparison with the measured spectra from Ref. [93] ($SrTiO_3$, $SrZrO_3$, $SrHfO_3$), Refs. [9,94] (Lanthanum series). For $SrMnO_3$ and $SrTcO_3$, we could not find any experimental reports in the literature. The agreement between the calculated and measured values are generally good. Unfortunately for the La series, the experimental data are limited to a small frequency window, which only allows for a comparison with the onset of the optical excitations. The cubic systems exhibit two prominent structures. According to the electronic structure properties discussed above, the first peak corresponds to the interband transition from O-2p to TM-t_{2g} states, and the second one is associated with the transition from O-2p to TM-e_g orbitals.

The energy separation between the two main peaks is predominantly determined by the crystal-field splitting. Using the GW QP energies, the independent particle approximation underestimates the energy seperation by 15%–20%: we obtained 1.5 eV (expt: 1.9 eV), 4.0 eV (expt: 5.1 eV), and 4.3 eV (expt: 4.9 eV) in $SrTiO_3$, $SrZrO_3$, $SrHfO_3$, respectively. We believe that this error is mainly related to the independent particle approximation which places the t_{2g} at too high energies. Including excitonic effects would lower these t_{2g} states [preliminary calculations on $SrTiO_3$ based on the Bethe-Salpeter equation (BSE) confirm this conclusion, in agreement with recent BSE data [102]]. The spectrum of $KTaO_3$ exhibits a less pronounced separation into two main peaks. This is due to the larger bandwidth of both the valence and conduction bands (see band structure in Fig. 11), which allows for more broadened optical transitions and the appearance of shoulders close to the main peaks.

For $NaOsO_3$, the calculated optical conductivity follows well the measurements of Lo Vecchio *et al.* [83]: the main absorption edge is mainly associated to charge-transfer excitations among Os-5d and O-2p states (see band structure in Fig. 11).

The variation of the optical properties and of the band gaps in the La series has been discussed in the seminal paper of Arima and co-workers. [9]. Also for this set of compounds, the agreement with the measured data is satisfactory, with the exception of $LaVO_3$ for which GW predicts a substantial

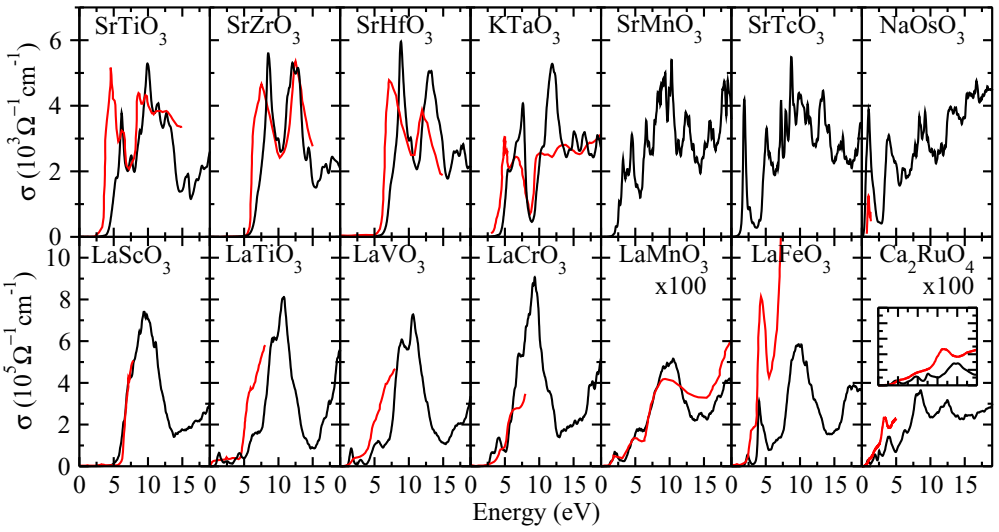

FIG. 12. Collection of calculated (black line) optical spectra along with available experimental curves (gray/red line); for $SrTiO_3$, $SrZrO_3$, and $SrHfO_3$ the experimental data are taken from Ref. [93], for $KTaO_3$ from Ref. [94], for $NaOsO_3$ from Ref. [83], for the La series from Ref. [9] ($LaMnO_3$ from Ref. [95]), and for Ca_2RuO_4 from Ref. [96]. For Ca_2RuO_4 the inset shows a zoom of the low-energy region. The calculated dielectric functions from which the optical conductivity spectra have been derived are shown in Fig. 13.

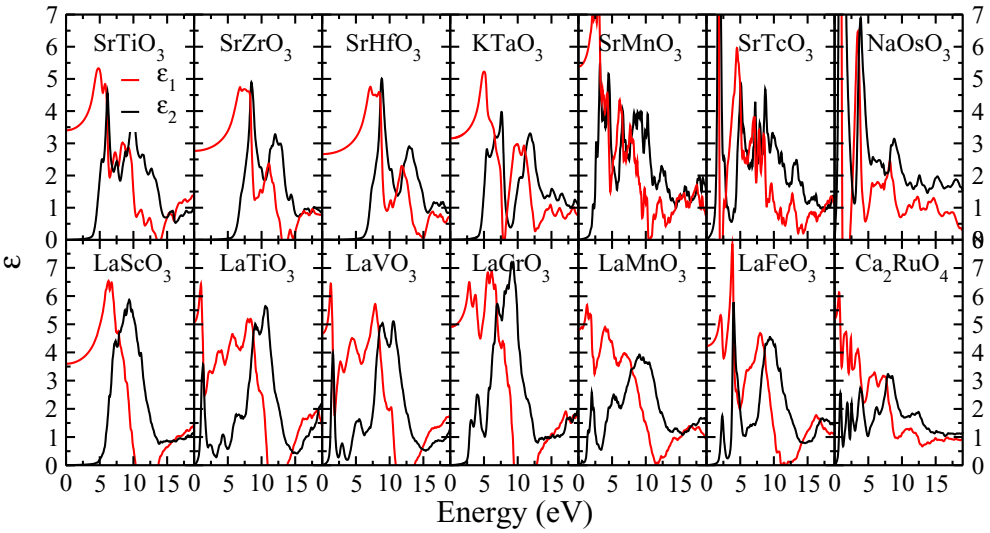

FIG. 13. Average of diagonal component of the real (ϵ_1) and imaginary (ϵ_2) parts of the dielectric function obtained by G_0W_0 for the entire materials data set studied in this work. The values of the static ion-clamped dielectric function ϵ_∞ are listed in Table VII.

blue-shift of the strongest excitation peak at about 2.5 eV. This discrepancy can again be related to the neglect of excitonic effects, which are strong for $p \rightarrow d$ transitions. However, the onset of the optical spectrum at 1.2 eV is well reproduced by theory and corresponds to the characteristic d-d transition, which is weak due to the low density of empty states at the bottom of the conduction band (see Fig. 11). $LaScO_3$ is a clear band insulator with the first (charge-transfer) optical excitation arising from the O-p to Sc-d transition; the experimental spectrum does not clearly show the tail at the bottom of the spectrum well visible in GW. We believe that the GW band structure is reliable in this respect, and that the onset of optical adsorption is not easily detected in the experiment. We therefore trust that our predicted band gap of 4.9 eV should be more reliable than the experimental estimate of 6.0 eV (see Table IV and Fig. 11). As the $3d$ states start to become occupied ($LaTiO_3$, $3d^1$), a Mott peak shows up in the low-energy region of the optical conductivity, but the overall spectra are still dominated by the intense charge-transfer peak located at about 9–10 eV (depending on the specific system). In $LaFeO_3$, a third relatively intense feature appears at 4.1 eV between the lowest Mott peak (2.3 eV) and the charge-transfer peak (9.8 eV), which can be assigned to the transition from the VBM to the group of bands centered at 4 eV above the Fermi level which have a mixed O-p and Fe-d character (see Fig. 11).

Finally, Ca_2RuO_4 displays four main peaks in the lowest part of the optical conductivity (i.e., in the energy window up to 5 eV for which experimental reports are available). On the basis of the electronic properties (bands and DOS) and following the labeling given in Fig. 11, we can tentatively assign the first peak at 1 eV to the $i \rightarrow a$ transition, the second two peaks at 2 and 2.5 eV can be interpreted as $j \rightarrow a$ and $i \rightarrow b$ excitations, and finally the broad and intense peak at about 4 eV should correspond to transition from the valence bands i, j to the main d bands b. While the more intense peak should have a clear charge-transfer character, the other transition might involve d-d Mott-type transitions [96]. However, a more quantitative and certain analysis of the specific type of transition would require beyond GW approaches such as the solution of the Bethe-Salpeter equation, which will be the topic of a future work. This comment applies to some degree to the interpretation of all spectra.

TABLE VII. Diagonal part of the static ($\omega = 0$, ion-clamped) dielectric matrix $\epsilon_\infty^{\alpha\beta}$ calculated by means of the G_0W_0 approximation.

Compound	ϵ_∞^{XX}	ϵ_∞^{YY}	ϵ_∞^{ZZ}
$SrTiO_3$	3.40	3.40	3.40
$SrZrO_3$	2.77	2.77	2.77
$SrHfO_3$	2.67	2.67	2.67
$KTaO_3$	3.16	3.16	3.16
$SrMnO_3$	5.26	5.26	5.61
$LaScO_3$	3.46	3.67	3.66
$LaTiO_3$	5.31	5.05	4.89
$LaVO_3$	3.83	6.51	3.70
$LaCrO_3$	4.90	4.89	4.96
$LaMnO_3$	4.83	4.58	5.02
$LaFeO_3$	4.23	4.19	4.28
$SrTcO_3$	7.53	7.46	7.66
Ca_2RuO_4	5.80	5.90	3.90
$NaOsO_3$	26.02	28.63	27.05

IV. CONCLUSIONS

In summary, in this study, we have assessed the performance and accuracy of the single-shot G_0W_0 approximation for the calculation of converged QP energies for transition metal perovskites using two different schemes (the basis-set correction procedure and the conventional nonextrapolated method) and inspected the dependence of the results on the type of PAW used in the computation (ultrasoft vs norm conserving). In order to draw general conclusions valid for different physical environments, we have performed a series of calculations on a TM perovskite data set comprising 14 compounds representative of the variety of properties characteristic of this class of materials: magnetic and nonmagnetic

systems, with and without structural distortions, with different occupancies ($d^0 \rightarrow d^5$) and spatial extension ($3d$, $4d$, and $5d$) of the outermost d shell, with band gap ranging from 0.1 eV ($NaOsO_3$) up to 6.1 eV ($SrHfO_3$) and different types of main optical excitations (Mott-Hubbard, charge-transfer, relativistic, and band insulators).

We reassert that the formally (mathematically) corrected procedure to obtain accurate QP energies requires a basis-set as well as a **k**-point correction. However, these corrections, in particular, the basis-set extrapolation, can become computationally prohibitive when combined with NC PAWs because norm-conserving pseudopotentials are generally constructed with a much larger number of plane waves compared to ultrasoft potentials (this is the case for Ca_2RuO_4, for which we could not perform NC-based calculations). On the other side, the use of US PAWs makes the basis-set corrections scheme computationally more advantageous than the nonextrapolated scheme because well-converged results can be achieved with few **k** points and the **k**-point correction requires only a small number of bands (and energy cutoffs). Even though the reliability of the conventional scheme, based on a progressive increase of the most important technical parameters influencing the convergence of the results (cutoff energy, number of bands, and number of **k** points) is not supported by a mathematical demonstration, our numerical results indicate that in most cases this scheme leads to reasonably converged QP energies very similar to those achieved by means of the basis-set correction scheme. This conclusion is of great practical importance as this allows to easily compute energy dispersion relations (band structures) and optical spectra, which cannot be computed using the basis-set correction method. The so-obtained optical spectra, based on the calculation of the frequency-dependent dielectric function (without the inclusion of excitonic effects), are in good agreement with experimentally available measurements and provide useful insight on the characterization of the most important optical transitions.

Concerning the difference between NC and US PAWs, the main source of inaccuracy in US-based calculations is the degree of norm violation for the d shell, which can be as large as 0.4–0.45 electrons for Mn and Fe. For most of the compounds considered in this study, this inaccuracy is somehow compensated by using a robust technical setup in US-based calculations [typically, $E_{\mathrm{pw}} = 500$–600 eV, $N = 500$ (in some cases up to 2000), and a $4 \times 4 \times 4$ **k**-point mesh]. In this respect, the most problematic compounds turned out to be $SrTiO_3$, for which US PAWs deliver a band gap 0.5 eV larger than the corresponding NC value. In general, particular care is required for $3d$ charge-transfer insulators ($p \rightarrow d$ transition). Also, late transition metals are more difficult than early transition metals since the d electrons become more localized towards the end of the d series.

Finally, a basic statistical analysis of our results indicates a strong correlation between the calculated and experimental band gap ($R^2 = 0.94$–0.95) as well as a very robust correlation between the GW and DFT gaps ($R^2 = 0.98$). Also, we found a correlation between the GW gap and the static dielectric function which could be particularly useful for automatic high-throughput calculations. As expected, the QP shift decreases with decreasing band gap, and this trend is characterized by two distinct behaviors: for the less electronically correlated d^0 p-d insulators and 4-5d compounds the QP shift is about 25% of the value of the gap, whereas for the more correlated $3d$ materials the QP shifts increase up to 50%–60%.

We hope that the results and conclusions of our work will serve as useful references for future GW calculations on complex transition metal oxides.

ACKNOWLEDGMENTS

This work was financially supported by the joint FWF (Austrian Science Fund) and Indian Department of Science and Technology (DST) project INDOX (Project No. I1490-N19), and by the FWF-SFB ViCoM (Grant No. F41). Computing time at the Vienna Scientific Cluster is greatly acknowledged.

APPENDIX: DETAILS ON THE EMPLOYED PAW POTENTIALS

Table VIII provides a list of radial cutoff parameters used for the construction of the PAW potentials used in the present study.

TABLE VIII. List of radial cutoff parameters (core radii, in atomic units) r_s, r_p, r_d, r_f for each angular quantum number and default E_{pw} for all type of potentials used in this work.

Element	PAW	r_s	r_p	r_d	r_f	E_{pw}
O	US	1.2	1.5	1.6	1.4	434
	NC	1.0	1.1	1.1		765
Na	US	1.4	2.2	2.2		373
	NC	1.2	2.2	2.2		467
K	US	1.7	2.0	2.5		249
	NC	1.0	1.8	2.1	2.1	633
Ca	US	1.6	1.9	2.2		281
	NC	0.9	1.7	1.9	2.1	771
Sc	US	1.7	1.7	1.9	2.0	379
	NC	0.9	1.5	1.9	1.9	778
Ti	US	1.7	1.7	2.0	2.0	384
	NC	0.9	1.4	1.9	1.9	785
V	US	1.8	1.7	1.9	2.0	384
	NC	0.8	1.3	1.9	1.9	800
Cr	US	2.8	2.5	2.5	2.8	219
	NC	0.8	1.2	1.9	1.9	819
Mn	US	1.6	1.7	1.9	1.9	385
	NC	1.6	1.3	1.9	1.9	781
Fe	US	1.5	1.7	1.9	2.0	388
	NC	1.5	1.7	1.9	1.9	786
Sr	US	1.7	2.1	2.5	2.5	225
	NC	1.1	2.0	2.3	2.1	543
Zr	US	1.3	1.8	2.0	2.1	346
	NC	1.0	1.9	2.1	1.9	637
Tc	US	2.0	1.8	2.0	2.1	351
	NC	0.9	1.9	2.1	1.9	639
Ru	US	2.0	1.8	2.0	2.1	348
	NC	0.9	1.9	2.1	1.9	660
La	US	1.6	1.8	2.2	2.5	314
Hf	US	1.5	1.9	2.2	2.5	283
	NC	2.2	2.0	2.2	1.9	576
Ta	US	1.5	1.9	2.2	2.5	286
	NC	2.1	2.0	2.2	1.9	584
Os	US	1.5	1.8	2.2	2.3	319
	NC	2.0	2.0	2.1	1.9	647

[1] R. von Helmolt, J. Wecker, B. Holzapfel, L. Schultz, and K. Samwer, Phys. Rev. Lett. **71**, 2331 (1993).
[2] M. B. Salamon and M. Jaime, Rev. Mod. Phys. **73**, 583 (2001).
[3] M. Imada, A. Fujimori, and Y. Tokura, Rev. Mod. Phys. **70**, 1039 (1998).
[4] J. G. Bednorz and K. A. Müller, Z. Phys. B **64**, 189 (1986).
[5] Y. Tokura, Phys. Today **56**(7), 50 (2003).
[6] A. Ohtomo and H. Y. Hwang, Nature (London) **427**, 423 (2004).
[7] K. Wang, J.-M. Liu, and Z. Ren, Adv. Phys. **58**, 321 (2009).
[8] C. Rao, J. Phys. Chem. B **104**, 5877 (2000).
[9] T. Arima, Y. Tokura, and J. B. Torrance, Phys. Rev. B **48**, 17006 (1993).
[10] J. Zhu, H. Li, L. Zhong, P. Xiao, X. Xu, X. Yang, Z. Zhao, and J. Li, ACS Catal. **4**, 2917 (2014).
[11] F. Dogan, H. Lin, M. Guilloux-Viry, and O. Peña, Sci. Technol. Adv. Mater. **16**, 020301 (2015).
[12] B. J. Kim, H. Jin, S. J. Moon, J.-Y. Kim, B.-G. Park, C. S. Leem, J. Yu, T. W. Noh, C. Kim, S.-J. Oh *et al.*, Phys. Rev. Lett. **101**, 076402 (2008).
[13] B. Kim, P. Liu, Z. Ergönenc, A. Toschi, S. Khmelevskyi, and C. Franchini, Phys. Rev. B **94**, 241113 (2016).
[14] G. Jackeli and G. Khaliullin, Phys. Rev. Lett. **102**, 017205 (2009).
[15] P. Liu, S. Khmelevskyi, B. Kim, M. Marsman, D. Li, X.-Q. Chen, D. D. Sarma, G. Kresse, and C. Franchini, Phys. Rev. B **92**, 054428 (2015).
[16] B. Kim, S. Khmelevskyi, I. I. Mazin, D. F. Agterberg, and C. Franchini, npj Quantum Mater. **2**, 37 (2017).
[17] P. Hohenberg and W. Kohn, Phys. Rev. **136**, B864 (1964).
[18] M. Van Schilfgaarde, T. Kotani, and S. Faleev, Phys. Rev. Lett. **96**, 226402 (2006).
[19] L. Hedin, Phys. Rev. **139**, A796 (1965).
[20] G. Strinati, H. J. Mattausch, and W. Hanke, Phys. Rev. Lett. **45**, 290 (1980).
[21] G. Strinati, H. J. Mattausch, and W. Hanke, Phys. Rev. B **25**, 2867 (1982).
[22] M. S. Hybertsen and S. G. Louie, Phys. Rev. Lett. **55**, 1418 (1985).
[23] M. S. Hybertsen and S. G. Louie, Phys. Rev. B **34**, 5390 (1986).
[24] W. G. Aulbur, L. Jonsson, and J. W. Wilkins, Solid State Phys. Adv. Res. Appl. **54**, 1 (1999).
[25] M. Shishkin and G. Kresse, Phys. Rev. B **75**, 235102 (2007).
[26] F. Fuchs, J. Furthmüller, F. Bechstedt, M. Shishkin, and G. Kresse, Phys. Rev. B **76**, 115109 (2007).
[27] J. Paier, M. Marsman, and G. Kresse, Phys. Rev. B **78**, 121201 (2008).
[28] B.-C. Shih, Y. Xue, P. Zhang, M. L. Cohen, and S. G. Louie, Phys. Rev. Lett. **105**, 146401 (2010).
[29] J. Klimeš, M. Kaltak, and G. Kresse, Phys. Rev. B **90**, 075125 (2014).
[30] J. Harl and G. Kresse, Phys. Rev. B **77**, 045136 (2008).
[31] T. Björkman, A. Gulans, A. V. Krasheninnikov, and R. M. Nieminen, Phys. Rev. Lett. **108**, 235502 (2012).
[32] A. Schindlmayr, Phys. Rev. B **87**, 075104 (2013).
[33] P. Liu, M. Kaltak, J. Klimeš, and G. Kresse, Phys. Rev. B **94**, 165109 (2016).
[34] M. Kim, G. J. Martyna, and S. Ismail-Beigi, arXiv:1707.06752.
[35] P. Umari, E. Mosconi, and F. De Angelis, Sci. Rep. **4**, 4467 (2015).
[36] M. R. Filip and F. Giustino, Phys. Rev. B **90**, 245145 (2014).
[37] I. E. Castelli, J. M. García-Lastra, K. S. Thygesen, and K. W. Jacobsen, APL Mater. **2**, 081514 (2014).
[38] M. Bokdam, T. Sander, A. Stroppa, S. Picozzi, D. D. Sarma, C. Franchini, and G. Kresse, Sci. Rep. **6**, 28618 (2016).
[39] C. Friedrich, S. Blügel, and A. Schindlmayr, Phys. Rev. B **81**, 125102 (2010).
[40] Y. Nohara, S. Yamamoto, and T. Fujiwara, Phys. Rev. B **79**, 195110 (2009).
[41] C. Franchini, A. Sanna, M. Marsman, and G. Kresse, Phys. Rev. B **81**, 085213 (2010).
[42] C. Franchini, R. Kovacik, M. Marsman, S. S. Murthy, J. He, C. Ederer, and G. Kresse, J. Phys.: Condens. Matter **24**, 235602 (2012).
[43] G. Kang, Y. Kang, and S. Han, Phys. Rev. B **91**, 155141 (2015).
[44] R. Kováčik, S. S. Murthy, C. E. Quiroga, C. Ederer, and C. Franchini, Phys. Rev. B **93**, 075139 (2016).
[45] S. Lany, Phys. Rev. B **87**, 085112 (2013).
[46] M. Sousa, C. Rossel, C. Marchiori, H. Siegwart, D. Caimi, J.-P. Locquet, D. J. Webb, R. Germann, J. Fompeyrine, K. Babich *et al.*, J. Appl. Phys. **102**, 104103 (2007).
[47] S. Ryee, S. W. Jang, H. Kino, T. Kotani, and M. J. Han, Phys. Rev. B **93**, 075125 (2016).
[48] J. He and C. Franchini, Phys. Rev. B **89**, 045104 (2014).
[49] M. J. van Setten, M. Giantomassi, X. Gonze, G.-M. Rignanese, and G. Hautier, Phys. Rev. B **96**, 155207 (2017).
[50] A. Gulans, J. Chem. Phys. **141**, 164127 (2014).
[51] J. He and C. Franchini, Phys. Rev. B **86**, 235117 (2012).
[52] J. He and C. Franchini, Phys. Rev. B **90**, 039907 (2014).
[53] H. E. Swanson, G. M. Ugrinic, R. K. Fuyat, and U. States, National Bureau Standards Circular 539 **3**, 73 (1954).
[54] A. J. Smith and A. J. E. Welch, Acta Crystallogr. **13**, 653 (1960).
[55] B. J. Kennedy, C. J. Howard, and B. C. Chakoumakos, Phys. Rev. B **60**, 2972 (1999).
[56] J. Sigman, D. P. Norton, H. M. Christen, P. H. Fleming, and L. A. Boatner, Phys. Rev. Lett. **88**, 097601 (2002).
[57] R. Søndenå, P. Ravindran, S. Stølen, T. Grande, and M. Hanfland, Phys. Rev. B **74**, 144102 (2006).
[58] S. Geller, Acta Crystallogr. **10**, 243 (1957).
[59] M. Cwik, T. Lorenz, J. Baier, R. Müller, G. André, F. Bourée, F. Lichtenberg, A. Freimuth, R. Schmitz, E. Müller-Hartmann, and M. Braden, Phys. Rev. B **68**, 060401 (2003).
[60] P. Bordet, C. Chaillout, M. Marezio, Q. Huang, A. Santoro, S.-W. Cheong, H. Takagi, C. Oglesby, and B. Batlogg, J. Solid State Chem. **106**, 253 (1993).
[61] U. States, C. P. Khattak, D. E. Cox, and R. February, Mater. Res. Bull. **12**, 463 (1977).
[62] J. B. A. A. Elemans, B. Van Laar, K. R. Van Der Veen, and B. O. Loopstra, J. Solid State Chem. **3**, 238 (1971).
[63] S. E. Dann, D. B. Currie, M. T. Weller, M. F. Thomas, and A. D. Al-Rawwas, J. Solid State Chem. **109**, 134 (1994).
[64] E. E. Rodriguez, F. Poineau, A. Llobet, B. J. Kennedy, M. Avdeev, G. J. Thorogood, M. L. Carter, R. Seshadri, D. J. Singh, and A. K. Cheetham, Phys. Rev. Lett. **106**, 067201 (2011).
[65] M. Braden, G. André, S. Nakatsuji, and Y. Maeno, Phys. Rev. B **58**, 847 (1998).
[66] Y. G. Shi, Y. F. Guo, S. Yu, M. Arai, A. A. Belik, A. Sato, K. Yamaura, E. Takayama-Muromachi, H. F. Tian, H. X. Yang *et al.*, Phys. Rev. B **80**, 161104(R) (2009).
[67] T. Takeda and S. Ōhara, J. Phys. Soc. Jpn. **37**, 275 (1974).
[68] G. Kresse and J. Hafner, Phys. Rev. B **47**, 558 (1993).

[69] G. Kresse and J. Furthmüller, Phys. Rev. B **54**, 11169 (1996).

[70] P. E. Blöchl, Phys. Rev. B **50**, 17953 (1994).

[71] J. P. Perdew, K. Burke, and M. Ernzerhof, Phys. Rev. Lett. **78**, 1396 (1997).

[72] S. L. Dudarev, G. A. Botton, S. Y. Savrasov, C. J. Humphreys, and A. P. Sutton, Phys. Rev. B **57**, 1505 (1998).

[73] M. Shishkin and G. Kresse, Phys. Rev. B **74**, 035101 (2006).

[74] W. Kang and M. S. Hybertsen, Phys. Rev. B **82**, 085203 (2010).

[75] T. Kato, Comm. Pure Appl. Math **10**, 151 (1957).

[76] In VASP the energy cutoff for the plane-wave expansion of the orbitals E_{pw} is controlled by the flag ENCUT, whereas the energy cutoff for the response function E^{χ}_{pw} is defined by the flag ENCUTGW and controls how many $\mathbf{G}$ vectors are included in the response function $\chi^{0}_{\mathbf{q}}(\mathbf{G},\mathbf{G}',\omega)$. ENCUTGW controls the basis set for the response functions in exactly the same manner as ENCUT does for the orbitals, in Hartree units: $N_{\mathrm{pw}} \approx \frac{\Omega}{2\pi^2}(2E_{\mathrm{pw}})^{3/2}$. In VASP the total number of plane waves N_{pw} is given by the maximum number of plane waves per irreducible $\mathbf{k}$ point.

[77] D. Nabok, A. Gulans, and C. Draxl, Phys. Rev. B **94**, 035118 (2016).

[78] See Supplemental Material at http://link.aps.org/supplemental/10.1103/PhysRevMaterials.2.024601 for a summary of all convergence tests for the band gap using both US and NC PAW.

[79] M. Takizawa, K. Maekawa, H. Wadati, T. Yoshida, A. Fujimori, H. Kumigashira, and M. Oshima, Phys. Rev. B **79**, 113103 (2009).

[80] Y. Tezuka, S. Shin, T. Ishii, T. Ejima, S. Suzuki, and S. Sato, J. Phys. Soc. Jpn. **63**, 347 (1994).

[81] K. Van Benthem, C. Elsässer, and R. H. French, J. Appl. Phys. **90**, 6156 (2001).

[82] Y. S. Lee, J. S. Lee, T. W. Noh, D. Y. Byun, K. S. Yoo, K. Yamaura, and E. Takayama-Muromachi, Phys. Rev. B **67**, 113101 (2003).

[83] I. L. Vecchio, A. Perucchi, P. Di Pietro, O. Limaj, U. Schade, Y. Sun, M. Arai, K. Yamaura, and S. Lupi, Sci. Rep. **3**, 2990 (2013).

[84] Z. Ergönenc, GW quasiparticle energies for transition metal oxide perovskites, Ph.D. thesis, University of Vienna, 2017.

[85] T. Saitoh, A. E. Bocquet, T. Mizokawa, H. Namatame, A. Fujimori, M. Abbate, Y. Takeda, and M. Takano, Phys. Rev. B **51**, 13942 (1995).

[86] G. E. Jellison, I. Paulauskas, L. A. Boatner, and D. J. Singh, Phys. Rev. B **74**, 155130 (2006).

[87] C. G. Fatuzzo, M. Dantz, S. Fatale, P. Olalde-Velasco, N. E. Shaik, B. Dalla Piazza, S. Toth, J. Pelliciari, R. Fittipaldi, A. Vecchione *et al.*, Phys. Rev. B **91**, 155104 (2015).

[88] H. Wang, F. Wu, and H. Jiang, J. Phys. Chem. C **115**, 16180 (2011).

[89] M. Shishkin, M. Marsman, and G. Kresse, Phys. Rev. Lett. **99**, 246403 (2007).

[90] S. Curtarolo, G. L. W. Hart, M. B. Nardelli, N. Mingo, S. Sanvito, and O. Levy, Nat. Mater. **12**, 191 (2013).

[91] J. He and C. Franchini, J. Phys.: Condens. Matter **29**, 454004 (2017).

[92] A. A. Mostofi, J. R. Yates, G. Pizzi, Y.-S. Lee, I. Souza, D. Vanderbilt, and N. Marzari, Comput. Phys. Commun. **185**, 2309 (2014).

[93] D. Lee, Y and Y. K. Seo, J. Korean Phys. Soc. **56**, 366 (2010).

[94] L. G. A. M. Mamedov, Fiz. Tverd. Tela (Leningrad) **26**, 583 (1984) [Sov. Phys.: Solid States **26**, 583 (1984)].

[95] J. H. Jung, K. H. Kim, D. J. Eom, T. W. Noh, E. J. Choi, J. Yu, Y. S. Kwon, and Y. Chung, Phys. Rev. B **55**, 15489 (1997).

[96] J. H. Jung, Z. Fang, J. P. He, Y. Kaneko, Y. Okimoto, and Y. Tokura, Phys. Rev. Lett. **91**, 056403 (2003).

[97] E. Pavarini and E. Koch, Phys. Rev. Lett. **104**, 086402 (2010).

[98] J. He, M.-X. Chen, X.-Q. Chen, and C. Franchini, Phys. Rev. B **85**, 195135 (2012).

[99] C. Franchini, T. Archer, J. He, X.-Q. Chen, A. Filippetti, and S. Sanvito, Phys. Rev. B **83**, 220402 (2011).

[100] J. Mravlje, M. Aichhorn, and A. Georges, Phys. Rev. Lett. **108**, 197202 (2012).

[101] J. G. Vale, S. Calder, C. Donnerer, D. Pincini, Y. G. Shi, Y. Tsujimoto, K. Yamaura, M. M. Sala, J. van den Brink, A. D. Christianson, and D. F. McMorrow, arXiv:1707.05551.

[102] L. Sponza, V. Véniard, F. Sottile, C. Giorgetti, and L. Reining, Phys. Rev. B **87**, 235102 (2013).